Comparison of MR acquisition strategies for super-resolution reconstruction using the Bayesian mean squared error

M. Nicastro[1], B. Jeurissen[1,2], Q. Beirinckx[1], C. Smekens[3], D. H. J. Poot[4], J. Sijbers[1,2], and A. J. den Dekker[1,2]

[1]imec - Vision Lab, Dept of Physics, University of Antwerp, Antwerp, Belgium.
[2]μNEURO Research Centre of Excellence, University of Antwerp, Belgium.
[3]Siemens Healthcare NV/SA, Beersel, Belgium.
[4]Biomedical Imaging Group Rotterdam, Dept of Radiology and Medical Informatics, Erasmus Medical Center, Rotterdam, The Netherlands.

Abstract In multi-slice super-resolution reconstruction (MS-SRR), a high resolution image, referred to as the SRR image, is estimated from a series of multi-slice images with a low through-plane resolution. This work proposes a framework based on the Bayesian mean squared error of the Maximum A Posteriori estimator of an SRR image to compare the accuracy and precision of two commonly adopted magnetic resonance acquisition strategies in MS-SRR. The first strategy consists of acquiring a set of multi-slice images in which each image is shifted in the through-plane direction by a different, sub-pixel distance. The second consists of acquiring a set of multi-slice images in which each image is rotated around the frequency or phase-encoding axis by a different rotation angle. Results show that MS-SRR based on rotated multi-slice images outperforms MS-SRR based on shifted multi-slice images in terms of accuracy, precision and mean squared error of the reconstructed image.

1 Introduction

In conventional magnetic resonance imaging, a direct high resolution (HR) acquisition with a high signal-to-noise ratio (SNR) is often impractical due to the long scan time required. Previous studies have demonstrated the potential of multi-slice super-resolution reconstruction (MS-SRR) to address this issue by improving the inherent trade-off between resolution, SNR, and scan time [1]. The MS-SRR method consists of estimating an HR image, named SRR image, from a series of multi-slice images with a low through-plane resolution, hereafter referred to as the low resolution (LR) images [2].
Two acquisition strategies are more commonly adopted. The first consists of acquiring a set of LR images in which each image is shifted in the through-plane direction by a different, sub-pixel distance [3]. The second acquisition strategy consists of acquiring a set of LR images in which each image is rotated around the frequency or phase-encoding axis by a different rotation angle [4, 5]. The rotated scheme allows for a better sampling of the k-space compared to the shifted scheme since each LR image samples a different part of the k-space. Conversely, in the shifted scheme, all the LR images sample the same part of the k-space, causing the MS-SRR to rely exclusively on recovering the aliased frequencies in the slice-encoding direction.
The first comparison among MS-SRR acquisition protocols based on the two strategies was proposed in [4, 5]. A second comparison was proposed more recently in the context of fetal imaging, in which the segmentation quality of the SRR image was adopted as a performance criterion [6]. In both cases, the performance analysis focused on the non-regularized MS-SRR problem. However, MS-SRR estimation consists of solving an inverse problem, and regularization is required to find a stable solution [7]. Therefore, in this work, we extend the analysis to the regularized case, developing a framework in which the Bayesian mean squared error (BMSE) of the Maximum A Posteriori (MAP) estimator is proposed as a performance criterion [8]. The MAP estimator is built incorporating prior knowledge about the reconstruction target. The BMSE is chosen as a performance criterion to compare the acquisition strategies in terms of accuracy and precision for the class of reconstruction targets described by the prior distribution. The BMSE results are verified with Monte Carlo simulation experiments.

2 Materials and Methods

2.1 Super-resolution model

Let $\mathbf{r} \in \mathbb{R}^{N_r \times 1}$ be the vector containing the intensities of the noiseless HR target magnitude image. Furthermore, let $\mathbf{s}_m \in \mathbb{R}^{N_s \times 1}$, with $m = 1,..,M$, be the vector containing the intensities of the m-th noiseless LR multi-slice magnitude image. Then, $\mathbf{s}_m$ can be modeled as:

$$\mathbf{s}_m(\mathbf{r}) = \mathbf{D}(\mathrm{AF})\mathbf{B}\mathbf{G}(\Phi_m)\mathbf{r}, \tag{1}$$

with $\mathbf{G} \in \mathbb{R}^{N_r \times N_r}$, $\mathbf{B} \in \mathbb{R}^{N_r \times N_r}$, $\mathbf{D} \in \mathbb{R}^{N_s \times N_r}$ linear operators that describe a geometric transformation, blurring and down-sampling, respectively. $\mathbf{G}$ is a function of the geometric transformation parameter Φ_m, which represents the rotation angle or the shift of the m-th multi-slice image according to the acquisition strategy. $\mathbf{B}$ models the sampling function of the magnetic resonance imaging (MRI) acquisition method. For multi-slice acquisitions, the sampling function can be separated into three functions applied in orthogonal directions aligned with the MR image coordinates. The in-plane directions (frequency and phase-encoding) are modelled by a periodic sinc and the through-plane direction (slice-encoding) by a smoothed box. $\mathbf{D}$ is a function of the anisotropy factor AF, representing the ratio of the slice thickness to the in-plane resolution.
The sampling of the LR images can be expressed here as a matrix-vector multiplication $\mathbf{s}(\mathbf{r}) = \mathbf{A}\mathbf{r}$ where $\mathbf{s} =$

$[\mathbf{s}_1^{\mathrm{T}},...,\mathbf{s}_M^{\mathrm{T}}]^{\mathrm{T}} \in \mathbb{R}^{\mathrm{MN_s}\times 1}$ and $\mathbf{A} = [\mathbf{A}_1^{\mathrm{T}},...,\mathbf{A}_M^{\mathrm{T}}]^{\mathrm{T}} \in \mathbb{R}^{\mathrm{MN_s}\times \mathrm{N_r}}$ with $\mathbf{A}_m = \mathbf{D}(\mathrm{AF})\mathbf{BG}(\Phi_m) \in \mathbb{R}^{\mathrm{N_s}\times \mathrm{N_r}}$. For a detailed description of the implementation, we refer to [9].

2.2 Conditional data distribution

Let $\tilde{\mathbf{s}} \in \mathbb{R}^{\mathrm{MN_s}\times 1}$ be the vector containing the intensities of the M acquired magnitude LR images, subject to noise. Because of the relatively high SNR of the thick slices composing the LR images, the noise distribution can be well approximated by a zero-mean Gaussian distribution [10]. If all voxels are assumed to be statistically independent and the standard deviation of the noise σ to be temporally and spatially invariant, the conditional probability density function (PDF) of the data points $\mathrm{p}(\tilde{\mathbf{s}}|\mathbf{r})$ is equal to the product of the marginal PDFs of the individual data points and can be expressed as follows:

$$\mathrm{p}(\tilde{\mathbf{s}}|\mathbf{r}) \propto \exp\left(-\frac{1}{2\sigma^2}\left\|\tilde{\mathbf{s}}-\mathbf{s}(\mathbf{r})\right\|_2^2\right). \tag{2}$$

2.3 Prior distribution

The prior distribution is modelled as a stationary Gaussian Markov Random Field [11]. This corresponds with the assumption of a multivariate Gaussian prior of the form:

$$\mathrm{p}(\mathbf{r}) \propto \exp\left(-\frac{1}{2}(\mathbf{r}-\bar{\mathbf{r}})^{\mathrm{T}}\mathbf{K}^{-1}(\mathbf{r}-\bar{\mathbf{r}})\right), \tag{3}$$

parametrised in terms of its mean $\bar{\mathbf{r}}$ and precision (inverse-covariance) matrix $\mathbf{K}^{-1}$, which is sparse, positive definite, and encodes statistical assumptions regarding the value of each HR image voxel based on the values of its neighboring voxels. Let r_i be the i-th HR voxel and $\mathbf{r}_{\boldsymbol{\partial}_i} \in \mathbb{R}^{\mathrm{N_n}\times 1}$ the voxels from the neighborhood surrounding r_i, where $\mathrm{N_n}$ is the number of neighborhood voxels, and $\boldsymbol{\partial}_i$ represents the neighborhood voxels indices. We assume the conditional probability of the i-th HR voxel given the neighborhood voxels $\mathrm{p}(\mathrm{r}_i|\mathbf{r}_{\boldsymbol{\partial}_i})$ to be Gaussian and of the form:

$$\mathrm{p}(\mathrm{r}_i|\mathbf{r}_{\boldsymbol{\partial}_i}) \propto \exp\left(-\frac{\lambda^2}{2}\left(\mathrm{r}_i - \sum_{j\in\boldsymbol{\partial}_i}\alpha_j \mathrm{r}_j,\right)^2\right), \tag{4}$$

where $\boldsymbol{\alpha} = \{\alpha_j\}_{j=1}^{\mathrm{N_n}}$ is the vector of the so-called field potentials. It can be demonstrated [12] that Eq. (4) holds if and only if the joint PDF $\mathrm{p}(\mathbf{r})$ assumes the form in Eq. (3) with:

$$\mathbf{K}_{i,j}^{-1} = \lambda^2 \begin{cases} 1, & i=j, \\ -\alpha_j & j\in\boldsymbol{\partial}_i. \end{cases} \tag{5}$$

Therefore, the hyperparameters $\boldsymbol{\alpha}$, $\bar{\mathbf{r}}$, and λ characterize the prior distribution.

2.4 MAP estimator

The MAP estimator of $\mathbf{r}$ maximizes the posterior PDF $\mathrm{p}(\mathbf{r}|\tilde{\mathbf{s}})$ with respect to $\mathbf{r}$, where $\mathrm{p}(\mathbf{r}|\tilde{\mathbf{s}})$ is defined according to Bayes' theorem [8] as:

$$\mathrm{p}(\mathbf{r}|\tilde{\mathbf{s}}) \propto \mathrm{p}(\tilde{\mathbf{s}}|\mathbf{r})\mathrm{p}(\mathbf{r}). \tag{6}$$

Therefore, the MAP estimator assumes the form:

$$\begin{aligned}\hat{\mathbf{r}} &= \arg\max_{\mathbf{r}} \ln \mathrm{p}(\mathbf{r}|\tilde{\mathbf{s}}) \\ &= \arg\min_{\mathbf{r}} \frac{1}{\sigma^2}\|\tilde{\mathbf{s}}-\mathbf{A}\mathbf{r}\|_2^2 + (\mathbf{r}-\bar{\mathbf{r}})^{\mathrm{T}}\mathbf{K}^{-1}(\mathbf{r}-\bar{\mathbf{r}}),\end{aligned} \tag{7}$$

which admits the closed-form solution:

$$\hat{\mathbf{r}} = \left(\sigma^{-2}\mathbf{A}^{\mathrm{T}}\mathbf{A}+\mathbf{K}^{-1}\right)^{-1}\left(\sigma^{-2}\mathbf{A}^{\mathrm{T}}\tilde{\mathbf{s}}+\mathbf{K}^{-1}\bar{\mathbf{r}}\right). \tag{8}$$

2.5 Bayesian MSE

The BMSE is proposed as a performance criterion to compare the two MS-SRR acquisition protocols described in the introduction section. Let us first define the component-wise MSE of $\hat{\mathbf{r}}$ as:

$$\mathrm{MSE}(\mathbf{r})_j = \mathbb{E}_{\tilde{\mathbf{s}}}\left[(\hat{\mathbf{r}}-\mathbf{r})(\hat{\mathbf{r}}-\mathbf{r})^{\mathrm{T}}\right]_{j,j}, \tag{9}$$

where $\mathbb{E}_{\tilde{\mathbf{s}}}[.]$ is the expectation operator over $\tilde{\mathbf{s}}$. The MSE can be decomposed as the sum of a variance term and a squared bias term:

$$\mathrm{MSE}(\mathbf{r})_j = \Sigma_{j,j} + \left[\boldsymbol{\beta}(\mathbf{r})\boldsymbol{\beta}^{\mathrm{T}}(\mathbf{r})\right]_{j,j}, \tag{10}$$

where $\boldsymbol{\Sigma} \in \mathbb{R}^{\mathrm{N_r}\times\mathrm{N_r}}$ and $\boldsymbol{\beta} \in \mathbb{R}^{\mathrm{N_r}\times 1}$ are the covariance matrix and the bias vector of $\hat{\mathbf{r}}$, respectively. For the MAP estimator defined in the previous subsection, we have:

$$\boldsymbol{\Sigma} = \sigma^{-2}\mathbf{Q}\mathbf{A}^{\mathrm{T}}\mathbf{A}\mathbf{Q}, \tag{11}$$

$$\boldsymbol{\beta}(\mathbf{r}) = \mathbf{Q}\mathbf{K}^{-1}(\mathbf{r}-\bar{\mathbf{r}}), \tag{12}$$

with

$$\mathbf{Q} = \left(\sigma^{-2}\mathbf{A}^{\mathrm{T}}\mathbf{A}+\mathbf{K}^{-1}\right)^{-1}. \tag{13}$$

The BMSE of the estimator of $\mathbf{r}$ can now be defined from the MSE as [8]:

$$\mathrm{BMSE}(\mathbf{r})_j = \mathbb{E}_{\mathbf{r}}\left[\mathrm{MSE}(\mathbf{r})\right]_j, \tag{14}$$

where $\mathbb{E}_{\mathbf{r}}[.]$ is the expectation operator over $\mathbf{r}$. The BMSE can also be decomposed as the sum of a variance and a squared bias term, which can be linked to the MSE components as follows:

$$\begin{aligned}\mathrm{BMSE}(\mathbf{r})_j &= \mathbb{E}_{\mathbf{r}}[\boldsymbol{\Sigma}]_{j,j} + \mathbb{E}_{\mathbf{r}}\left[\boldsymbol{\beta}(\mathbf{r})\boldsymbol{\beta}^{\mathrm{T}}(\mathbf{r})\right]_{j,j} \\ &= \Sigma_{j,j} + \mathbb{E}_{\mathbf{r}}\left[\boldsymbol{\beta}(\mathbf{r})\boldsymbol{\beta}^{\mathrm{T}}(\mathbf{r})\right]_{j,j},\end{aligned} \tag{15}$$

where $\mathbb{E}_{\mathbf{r}}[\boldsymbol{\Sigma}] = \boldsymbol{\Sigma}$, since $\boldsymbol{\Sigma}$ does not depend on $\mathbf{r}$, and the squared bias term of the BMSE can be calculated as the expectation over $\mathbf{r}$ of the MSE squared bias component in Eq. (12):

$$\mathbb{E}_{\mathbf{r}}\left[\boldsymbol{\beta}(\mathbf{r})\boldsymbol{\beta}^{\mathrm{T}}(\mathbf{r})\right] = \mathbf{Q}\mathbf{K}^{-1}\mathbf{Q}. \tag{16}$$

To simplify the notation, we define:

$$\mathbf{RBMSE} = \left\{ \sqrt{\mathrm{BMSE}(\mathbf{r})_j} \right\}_{j=1}^{\mathrm{N_r}}, \tag{17}$$

$$\mathbf{v} = \left\{ \sqrt{\Sigma_{j,j}} \right\}_{j=1}^{\mathrm{N_r}}, \tag{18}$$

$$\mathbf{b} = \left\{ \sqrt{\mathbb{E}_{\mathbf{r}} \left[\boldsymbol{\beta}(\mathbf{r}) \boldsymbol{\beta}^{\mathrm{T}}(\mathbf{r}) \right]_{j,j}} \right\}_{j=1}^{\mathrm{N_r}}, \tag{19}$$

where the dependency of **RBMSE** and **b** on **r** was omitted. In the following sections, we will refer to **v** and **b** as the standard deviation component and absolute bias component of the BMSE, respectively.

2.6 Acquisition protocols

The acquisition protocols are shown in Table 1. For all the protocols we fixed $\mathrm{M/AF} = 2$. This choice ensures that the MS-SRR estimation problem is not under-determined ($\mathrm{M/AF} \geq 1$) [5] and that the *k*-space is efficiently sampled when the LR images are acquired with the rotated scheme $\left(\mathrm{M} > \frac{\pi}{2}\mathrm{AF}\right)$ [13]. Furthermore, it ensures that all the acquisition protocols require the same scan time. The HR protocol is included as a reference and represents a conventional multi-slice acquisition with $\mathrm{AF} = 1$, repeated twice. In the SRrot protocols, the acquired images are simulated rotated around the phase-encoding axis. The rotation angles are uniformly distributed in the open interval $[0, 180)$, with steps of $180/\mathrm{M}^\circ$. In the SRsh protocols, the acquired images are simulated shifted in the through-plane direction. The shifts, expressed in HR voxel indices, are uniformly distributed in the closed interval $[-\mathrm{AF}(\mathrm{M}-1)/(2\mathrm{M}), \mathrm{AF}(\mathrm{M}-1)/(2\mathrm{M})]$, with steps of $\mathrm{AF/M}$.

Protocols	AF	M	$\boldsymbol{\Phi} = \{\Phi_m\}_{m=1}^{M}$
HR	1	2	[0, 0]°
$\mathrm{SRrot_1}$	1	2	[0, 90]°
$\mathrm{SRrot_2}$	2	4	[0, 45, 90, 135]°
$\mathrm{SRrot_3}$	3	6	[0, 30, 60, 90, 120, 150]°
$\mathrm{SRrot_4}$	4	8	[0, 22.5, 45, 67.5, 90, 112.5, 135, 157.5]°
$\mathrm{SRsh_1}$	1	2	[-0.25, 0.25]
$\mathrm{SRsh_2}$	2	4	[-0.75, -0.25, 0.25, 0.75]
$\mathrm{SRsh_3}$	3	6	[-1.25, -0.75, -0.25, 0.25, 0.75, 1.25]
$\mathrm{SRsh_4}$	4	8	[-1.75, -1.25, -0.75, -0.25, 0.25, 0.75, 1.25, 1.75]

Table 1: MS-SRR acquisition protocols.

2.7 Prior hyperparameters estimation

The translational symmetry of the acquisition strategies along the phase-encoding axis was exploited to evaluate the framework in 2D, thereby reducing computational complexity and memory consumption. In order to estimate the prior hyperparameters, a training dataset was generated. The dataset, composed of 500 synthetic noiseless HR 2D T1-weighted (T1-w) magnitude brain images of size 120×120, was simulated starting from 10 anatomical brain models available in the Brainweb database [14]. The images, each representing an independent realization of **r**, were simulated with different acquisition planes (sagittal, transverse, and coronal) and T1 contrast. Additionally, each image was slightly rotated to simulate different head orientations, where the rotation angles were independently sampled from a Gaussian distribution with mean 0 and standard deviation 1. The hyperparameters $\boldsymbol{\alpha}$ and λ were estimated from the images within the training dataset using the kernel-regression approach proposed in [15] from the non-zero voxels within the training dataset and their respective 3×3 neighborhoods. All the elements of the prior mean $\bar{\mathbf{r}}$ were set equal to the mean intensity of the non-zero voxels within the training dataset. The choice of setting the prior mean of all voxels equal to the same constant ensures the prior to be invariant to the positioning (translation) of the head within the field of view.

2.8 Protocols comparison

We assumed the images acquired with the HR protocol to have an $\mathrm{SNR} = 20$, where the SNR was defined as the ratio of the mean intensity of the brain voxels within the training dataset to the standard deviation of the noise. The thus obtained standard deviation of the noise was fixed for all protocols, resulting in an SNR that increases with AF, as more signal is received from thicker slices. The BMSE as well as its separate squared bias and variance components were computed for each acquisition protocol using the closed-form expressions derived in the subsection 2.5.

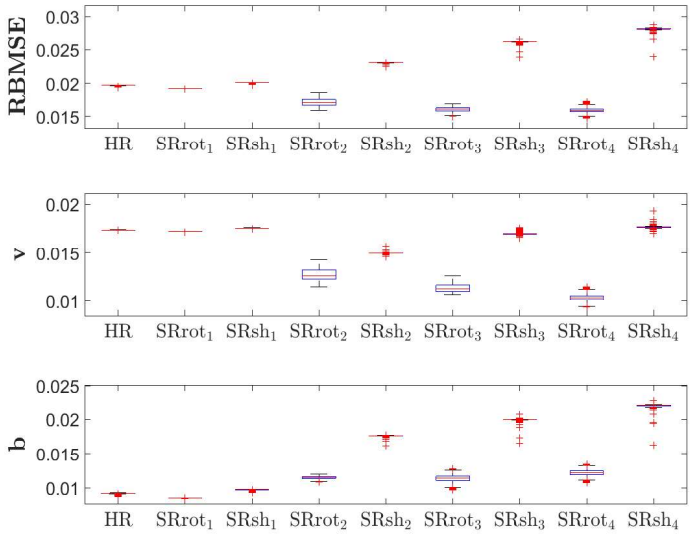

Figure 1: Boxplots of the **RBMSE** and of the BMSE standard deviation component **v** and absolute bias component **b** computed inside a ROI.

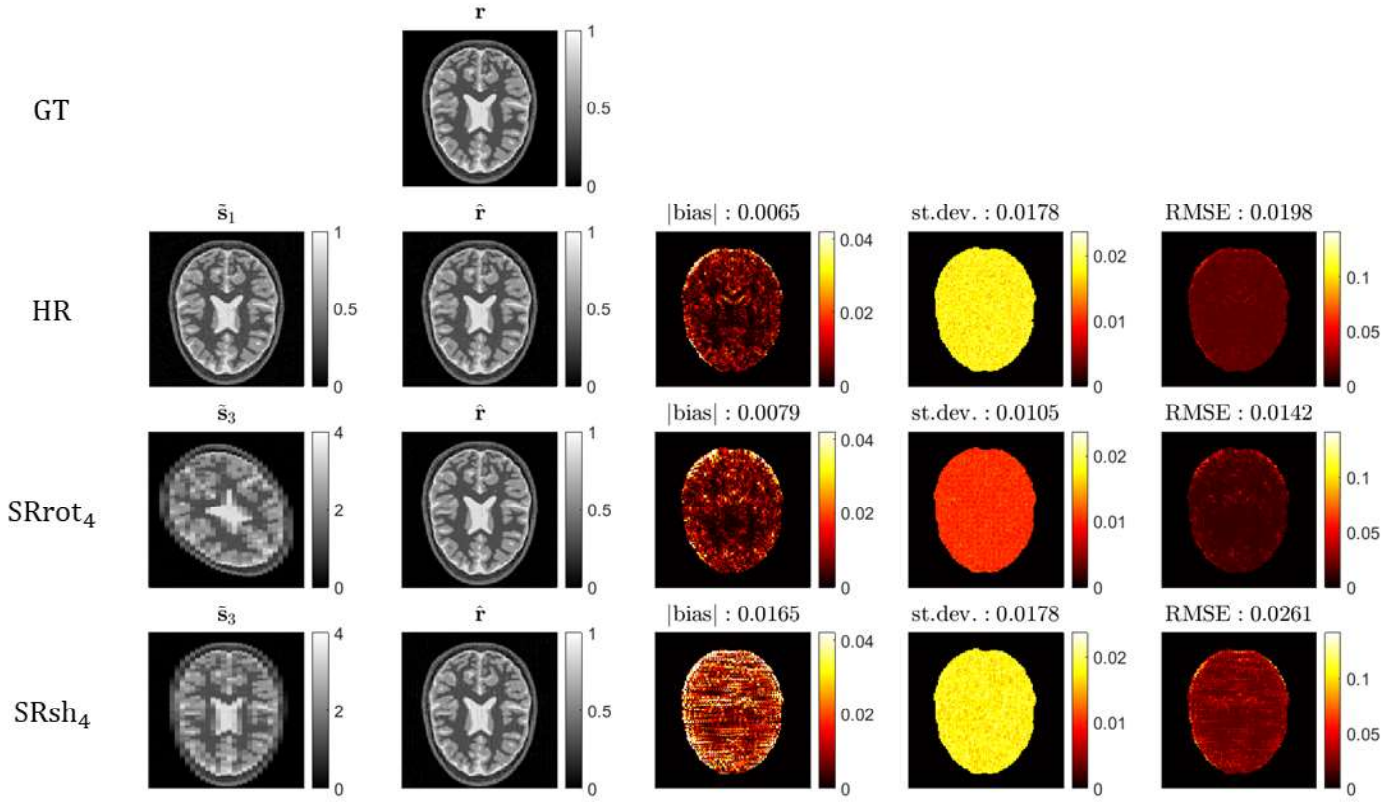

Figure 2: Monte Carlo simulation results for the protocols HR, SRrot4 and SRsh4. $\tilde{\mathbf{s}}_n$, $\mathbf{r}$, $\hat{\mathbf{r}}$ represent the n-th acquired LR image, ground truth image and estimated SRR image, respectively. The mean absolute bias, the mean standard deviation, and the mean RMSE values computed inside the brain mask are reported.

2.9 Monte Carlo simulation

A 2D T1-w axial brain slice, initially excluded from the training dataset, was used as ground truth (GT). The acquisition process was simulated for the protocols HR, SRrot_4 and SRsh_4 using the MS-SRR forward model in Eq. (1), and the simulated images were corrupted with noise, as described in the previous subsection. The Conjugate Gradient method [16] was used to solve the minimization problem in Eq. (7). Absolute bias, standard deviation, and RMSE maps were computed from 100 noise realizations for each protocol.

3 Results and Discussion

The distributions of the RBMSE maps inside a region of interest (ROI) for all the acquisition protocols are reported in Fig. 1, where the ROI was defined as the part of the field of view common to all the acquired images of all the acquisition protocols. The SR protocols based on the rotated acquisition scheme SRrot showed lower RBMSE values compared to the HR protocol and the SR protocols based on the shifted acquisition scheme SRsh. Increasing the AF led to an RBMSE improvement for the SRrot protocols, while the SRsh protocols showed the opposite trend. This difference is caused by both the absolute bias component **b**, which increases severely with AF for the SRsh protocols, and the standard deviation component **v**, which reduces significantly with AF for the SRrot protocols. The results of the Monte Carlo simulation for the HR, SRrot_4 and SRsh_4 protocols are reported in Fig. 2. The close agreement between the Monte Carlo results and the BMSE results demonstrates that the prior distribution was able to describe the statistics of the target image. The observed difference in terms of RBMSE between the SRrot and SRsh protocols (up to a factor 2, approximately) suggests that adopting the rotated acquisition scheme over the shifted scheme in a MS-SRR experiment can lead to a substantially reduced scan time while preserving the same MSE of the estimated SRR image. The main limitations of this work are the assumptions that the image registration parameters and the point spread function of the MRI acquisition process are perfectly known. The effect on the current analysis of nonidealities, such as motion artifacts and inconsistent modelling of the slice profile, will be the subject of future work. Additionally, real data experiments will be included to validate the proposed framework. Furthermore, we plan to extend the current study by applying the optimal experimental design theory principles to find the optimal acquisition settings for an MS-SRR experiment in terms of BMSE.

4 Conclusion

The potential of the BMSE framework for optimal experiment design was demonstrated by comparing two conventionally adopted MS-SRR acquisition protocols. The MS-acquisition strategy based on rotated multi-slice images out-

performed the strategy based on shifted images in terms of estimation accuracy and precision, evaluated by the squared bias and variance terms of the BMSE of the MAP estimator, respectively. The results confirmed and extended the conclusion of [4, 5] and [6] to regularized MS-SRR.

5 Acknowledgments

The project B-Q MINDED has received funding from the European Union's Horizon 2020 research and innovation programme under the Marie Sklodowska-Curie grant agreement No 764513. B. J. is a postdoctoral fellow of FWO Vlaanderen.

References

[1] E. Plenge, D. H. J. Poot, M. Bernsen, et al. "Super-resolution methods in MRI: can they improve the trade-off between resolution, signal-to-noise ratio, and acquisition time?" *Magn. Reson. Med.* 68.6 (2012), pp. 1983–1993. DOI: 10.1002/mrm.24187.

[2] E. Van Reeth, I. W. K. Tham, C. H. Tan, et al. "Super-resolution in magnetic resonance imaging: A review". *Concept. Magn. Reson. A* 40A.6 (2012), pp. 306–325. DOI: 10.1002/cmr.a.21249.

[3] H. Greenspan, G. Oz, N. Kiryati, et al. "MRI inter-slice reconstruction using super-resolution". *Magn Reson Imaging* 20.5 (2002), pp. 437–446. DOI: 10.1016/s0730-725x(02)00511-8.

[4] R. Z. Shilling, S. Ramamurthy, and M. E. Brummer. "Sampling strategies for super-resolution in multi-slice MRI". *15th IEEE ICIP*. 2008, pp. 2240–2243. DOI: 10.1109/ICIP.2008.4712236.

[5] R. Z. Shilling, T. Q. Robbie, T. Bailloeul, et al. "A Super-Resolution Framework for 3-D High-Resolution and High-Contrast Imaging Using 2-D Multislice MRI". *IEEE Trans. Med. Imaging* 28.5 (2009), pp. 633–644. DOI: 10.1109/TMI.2008.2007348.

[6] N. Askin, L. Levy, J. Sadealmeida, et al. "Super-resolution reconstruction applied to neonatal MRI: orthogonal vs through-plane slice shift MRI acquisition and segmentation". *27th ISMRM*. 2019.

[7] M. M. Khattab, A. M. Zeki, A. A. Alwan, et al. "Regularization-based multi-frame super-resolution: A systematic review". *J. King Saud Univ. Comput. Inf. Sci.* 32.7 (2020), pp. 755 –762. DOI: 10.1016/j.jksuci.2018.11.010.

[8] H. Van Trees. *Detection Estimation and Modulation Theory*. New York: Wiley, 1968.

[9] D. H. J. Poot, V. Van Meir, and J. Sijbers. "General and Efficient Super-Resolution Method for Multi-slice MRI". *MICCAI 2010*. Springer Berlin Heidelberg, 2010, pp. 615–622. DOI: 10.1007/978-3-642-15705-9_75.

[10] A. J. den Dekker and J. Sijbers. "Data distributions in magnetic resonance images: A review". *Phys. Med.* 30.7 (2014), pp. 725 –741. DOI: 10.1016/j.ejmp.2014.05.002.

[11] J. Bardsley. "Gaussian Markov random field Priors for inverse problems". *Inverse Problems and Imaging* 2 (2013). DOI: 10.3934/ipi.2013.7.397.

[12] H. Rue and L. Held. *Gaussian Markov Random Fields: Theory and Applications*. Chapman and Hall/CRC, 2005. DOI: 10.1201/9780203492024.

[13] G. Van Steenkiste, B. Jeurissen, J. Veraart, et al. "Super-resolution reconstruction of diffusion parameters from diffusion-weighted images with different slice orientations". *Magn. Reson. Med.* 75.1 (2016), pp. 181–195. DOI: 10.1002/mrm.25597.

[14] C. A. Cocosco, V. Kollokian, R. K. S. Kwan, et al. "BrainWeb: Online Interface to a 3D MRI Simulated Brain Database". *NeuroImage* 5 (1997), p. 425.

[15] R. Cusani and E. Baccarelli. "Identification of 2-D noncausal Gauss-Markov random fields". *IEEE Trans. Signal Process.* 44.3 (1996), pp. 759–764. DOI: 10.1109/78.489058.

[16] M. R. Hestenes and E. Stiefel. "Methods of conjugate gradients for solving linear systems". *J. Res. Nat. Bur. Stand.* 49.6 (1952), pp. 409–435. DOI: 10.6028/jres.049.044.